




Polarization-sensitive optical coherence tomography in end-stage lung diseases: an *ex vivo* pilot study

JOY WILLEMSE,^{1,7}  REINIER R. WENER,^{2,3,5,7} FABIO FEROLDI,^{1,4}  MARGHERITA VASELLI,¹ JOHANNA M. KWAKKEL-VAN ERP,^{2,5} EDUARD A. VAN DE GRAAF,⁵ ERIK THUNNISSEN,⁶ AND JOHANNES F. DE BOER^{1,*} 

¹LaserLaB, Department of Physics and Astronomy, Vrije Universiteit Amsterdam, Amsterdam, The Netherlands

²Department of Pulmonology, Antwerp University Hospital, Edegem, Belgium

³Department of Thoracic Oncology, Antwerp University Hospital, Edegem, Belgium

⁴Currently with the School of Optometry, University of California, Berkeley, California 94720, USA

⁵Department of Pulmonary Diseases, Utrecht University Medical Center, Utrecht, The Netherlands

⁶Department of Pathology, Amsterdam University Medical Center, Location VUmc, Amsterdam, The Netherlands

⁷These authors contributed equally

*j.f.de.boer@vu.nl

Abstract: A non-invasive diagnostic tool to assess remodeling of the lung airways caused by disease is currently missing in the clinic. Measuring key features such as airway smooth muscle (ASM) thickness would increase the ability to improve diagnosis and enable treatment evaluation. In this research, polarization-sensitive optical coherence tomography (PS-OCT) has been used to image a total of 24 airways from two healthy lungs and four end-stage diseased lungs *ex vivo*, including fibrotic sarcoidosis, chronic obstructive pulmonary disease (COPD), fibrotic hypersensitivity pneumonitis, and cystic fibrosis. In the diseased lungs, except COPD, the amount of measured airway smooth muscle was increased. In COPD, airway smooth muscle could not be distinguished from surrounding collagen. COPD lungs showed increased alveolar size. 3D pullbacks in the same lumen provided reproducible assessment of airway smooth muscle (ASM). Image features such as thickened ASM and size/presence of alveoli were recognized in histology. The results of this study are preliminary and must be confirmed with further *ex vivo* and *in vivo* studies. PS-OCT is applicable for *in vivo* assessment of peribronchial and peribronchiolar lung structures and may become a valuable tool for diagnosis in pulmonology.

© 2021 Optical Society of America under the terms of the [OSA Open Access Publishing Agreement](#)

1. Introduction

Optical coherence tomography (OCT) is an imaging tool mainly used in ophthalmology to create 3-dimensional cross-sectional images with micrometer resolution. In pulmonology, OCT is a new emerging technology. Catheter-based OCT can easily be applied using conventional bronchoscopy. Airway wall layers of normal lung tissue can be identified and quantified using OCT [1]. OCT has revealed the presence of lung cancer by loss of the usual structured layer of the airway wall [2–4]. In obstructive lung diseases, airway wall layers and related structural remodeling were identified [5,6]. OCT has been shown to be useful in interstitial lung disease (ILD) diagnosis *in vivo* with histological confirmation, specifically to differentiate usual interstitial pneumonitis (UIP) from idiopathic pulmonary fibrosis (IPF) [7,8].

Polarization-sensitive OCT (PS-OCT) is an extension of conventional OCT, providing additional contrast based on birefringence properties of fibrous structures [9–11]. PS-OCT has been used

to show contrast between lung tumor and tumor-associated fibrosis [12,13]. Adams *et al.* [14] showed that PS-OCT can detect the airway wall smooth muscle (ASM) cell layer, indicating that it might be a valuable tool for the assessment of airway wall remodeling. Recently, a reduction of ASM in lungs imaged before and after undergoing bronchial thermoplasty was shown with PS-OCT *in vivo* in a canine model [15] and an asthma patient [16].

In this study, multiple diseased lungs and healthy lungs were imaged *ex vivo* to investigate their distinguishing features in PS-OCT imaging. Cross-sectional lung lumen histology of the samples was used to confirm PS-OCT image features. This study was performed *ex vivo*, given the difficulty in finding the exact location where a biopsy was taken in a volumetric PS-OCT scan. Moreover, biopsies taken *in vivo* do not provide a cross-sectional view of the lung lumen, which is the scan orientation of endoscopic OCT.

2. Methods

2.1. Tissue specimens

Tissue from end-staged diseased explanted human lungs and healthy lungs was measured. The diseased lungs included one COPD lung, one FS lung, one fHP lung and one CF lung. Additionally, two healthy donor human lungs were imaged. A total of six lungs were imaged.

Lung specimen imaging was performed on fresh material within 24 hours after surgical resection. Each lung was sliced up in several parts. At the cutting edge, a small airway (diameter ~2 mm) was selected for PS-OCT imaging. This airway was marked at the edge with ink such that the correct airway would be sectioned for histology. The lungs were not inflated. The airways used for imaging were mostly obtained from the distal regions. Diagnoses are described in Table 1. All patients received a double or single sided lung transplantation due to end-staged lung disease with a very poor prognosis. All patients gave informed consent to examine their explanted lung for PS-OCT imaging *ex vivo*. The study was approved by the human Medical Ethics Committee of the University Medical Center Utrecht (TC biobanking protocol number 16-346).

Table 1. Overview of lung types and results

Diagnosis	Age, sex	Alveoli size within scan	ASM area per frame (% mean \pm STD)	ASM area per pullback (% mean \pm SEM)	Mean pullback length (mm)
Healthy, non-smoker, subarachnoid bleeding	41 M	Small	0.8 \pm 0.7	0.80 \pm 0.12	21.6 \pm 3.7
Healthy, non-smoker, subarachnoid bleeding	37 M	Small	0.5 \pm 0.4	0.45 \pm 0.07	14.0 \pm 9.0
COPD/alpha-1 antitrypsin deficiency	59 F	Large	% not available	% not available	24.3 \pm 11.1
Fibrotic sarcoidosis	58 F	Absent	4.6 \pm 2.0	4.4 \pm 0.5	16.4 \pm 4.5
Fibrotic hypersensitivity pneumonitis	44 F	Absent	3.0 \pm 1.8	2.8 \pm 0.4	21.9 \pm 4.9
Cystic fibrosis	32 F	Mostly absent	2.6 \pm 1.8	2.2 \pm 0.4	22.5 \pm 16.0

2.2. PS-OCT measurements

The PS-OCT catheter was pushed gently into the airway until resistance was felt. Hereafter, the catheter was automatically pulled back with a constant speed of 2 mm/s, while recording PS-OCT images. From every lung, four airways were selected for a PS-OCT measurement. In total 24 airways were measured. All selected airways were measured twice to test the repeatability of the technique. The lengths of the acquired pullbacks were between 2.9 and 43.2 mm, with a mean

pullback length of 20.1 mm. The reduced length of some pullbacks was due to the slicing of the lungs close to the airway end.

2.3. Matching histology with PS-OCT

After imaging, the ink-marked airways were cut in a total of 186 tissue samples for histology staining. The samples were fixed by submerging in 10% formalin, processed, sectioned according to standard histology procedures, and stained with hematoxylin–eosin. A histologic sample was taken every 3 mm along the imaged airway lumen. The images from both techniques were visually compared taking into account the pullback position and spacing between histopathology and matches were made. A match between histology and PS-OCT images could not be found for every airway in all lung types due to absence of characteristic airway features. However, at least one confident match between histology images and PS-OCT images was obtained for each lung type. A total of 21 confident matches were found, and more ‘less-confident’ matches were found. Characterizing features as cartilages, blood vessels, and smooth muscle areas were marked on 12 histologic images of the confident matches by an independent pulmonary pathologist.

2.4. Setup PS-OCT

The PS-OCT setup has been described in detail by Feroldi *et al.* [17]. The distal scanning catheter is a motorized endoscopic probe with a diameter of 1.35 mm, rotating at 52 rotations/s. The axial resolution of the system is 12 μm in tissue ($n = 1.4$). The lateral resolution is determined by the focal spot size, which is 13 μm . Total imaged tissue depth is around 1.3 mm.

2.5. Data processing

Initial processing steps have been described by Feroldi *et al.* [17]. Images based on the depth-resolved attenuation coefficient (AC) of the tissue are calculated based on the algorithm developed by Vermeer *et al.* [18]. AC images show superior architectural contrast compared to standard structural OCT (intensity) images [17], which is why AC images are used throughout the manuscript. A comparison of the intensity and AC cross sectional images can be found in the [Supplement 1](#).

Optic axis orientation images were extracted using the differential Mueller matrix method introduced by Villiger *et al.* [19]. This method was adapted to correct for the presence of preceding birefringent layers of tissue with a different optic axis [20]. The differential Mueller matrix is used to calculate the birefringence vector as follows:

$$\mathbf{\Gamma} = \frac{1}{2} \begin{bmatrix} m_{34} - m_{43} \\ m_{24} - m_{42} \\ m_{32} - m_{23} \end{bmatrix}, \quad (1)$$

where $m_{i,j}$ are the differential Mueller matrix elements of the i -th row and j -th column. The direction of this vector gives the apparent optic axis, and the length of this vector gives the phase retardation. An assumption here is that we are always dealing with purely birefringent matrices. To assess the validity of this assumption, we define the dM-error as:

$$\text{Error}_{\text{dM}} = \left\| \begin{bmatrix} m_{34} + m_{43} \\ m_{24} + m_{42} \\ m_{32} + m_{23} \end{bmatrix} \right\|. \quad (2)$$

This metric expressed as a rotation angle is zero for a purely birefringent material, because the elements of the differential Mueller matrix that are paired are then equal with opposite sign.

However, it deviates from zero in tissue regions containing depolarization and high noise, and can be used as an exclusion criteria for these effects in birefringence-based images.

Optic axis images were also corrected for the changing input polarization state due to the rotating mirror. The extracted tissue optic axis remained relative with a constant offset within one pullback, but the constant offset varied from pullback to pullback. In these images, the color-coding is rotated (a constant offset was applied to all orientations within one pullback) such that ASM has the same color in all datasets.

Evaluating the entropy/uniformity of the optic axis can provide better contrast for fibrous structures in PS-OCT imaging [21] with less dependence on depth [22]. Optic axis uniformity (OAxU) [21] was extracted by evaluating the spatial uniformity of the optic axis over a 3D Gaussian kernel ($4 \times 18 \times 2$ pixels) of the sample. Optic axis orientation images are shaded when OAxU is lower than 0.6, to better visualize the orientations of birefringent structures among non-birefringent structures with a random optic axis.

In all images, the part of the tissue not optically accessible due to the presence of the copper wires feeding current to the motor are masked in gray. In the birefringence-based images, pixels are also grayed out if they were not surrounded by at least 50 pixels (in a 4-connected neighborhood) which had an intensity level higher than approximately 8 dB above the noise floor, and a dM-error less than 0.2 radians. The endoscope sheath is segmented automatically and displayed in black in the images.

ASM was automatically segmented as pixels with OAxU higher than 0.7 and with the same orientation $[-34^\circ, +34^\circ]$ throughout the C-scan. ASM percentages are calculated for each frame as the number of segmented pixels divided by the number of pixels below the catheter sheath that are not shadowed by the wires in the image.

The average amount of ASM and its spread are reported using two slightly different approaches. The first approach is to report the values per frame. The standard deviations of all frames that have been measured in all pullbacks of the lung type show the biological variability. It includes both the measurement error and natural variation. In practice, the average ASM content measured in each airway will be of most interest, which is why the second approach is to report the values per pullback. In the second approach, the average amount of ASM is calculated first across the individual pullbacks. The mean of the eight pullbacks per lung type is different from the mean of all frames, because the lengths of the pullbacks are not equal. Instead of the standard deviation, the standard error of the mean (SEM) per lung type is reported for the $N = 8$ measurements, assuming that average ASM content is equal between different airways in the same lung.

To evaluate the repeatability of the ASM percentages extracted within the two consecutive pullbacks acquired in the same airway the two pullbacks need to be overlaid to correct for small differences in starting position and pullback speed. The frame numbers of the longest pullback were translated and squeezed such that the peaks match between the two pullbacks. Examples of this procedure can be found in the [Supplement 1](#). The absolute difference in ASM percentage is calculated between the shorter pullback and the remapped longer pullback for 24 pairs (4 pairs per lung type). The relative percent difference to the ASM% is calculated as:

$$\text{Diff}_{\%} = \frac{|\text{ASM}_{\%,1} - \text{ASM}_{\%,2}|}{\frac{1}{2}(\text{ASM}_{\%,1} + \text{ASM}_{\%,2})} \cdot 100. \quad (3)$$

The absolute ASM% difference and relative percent difference are analyzed per frame and per pullback as well.

3. Results

The mean ASM percentages per frame and per pullback are given in Table 1 for all lung types. No ASM percentage was calculated for COPD samples, because the presence of collagen, cartilages,

and/or blood vessels obscured the signal from ASM. This is further explained in the separate section on COPD.

Figure 1 shows the segmented ASM content per frame for each lung type summarized in box plots.

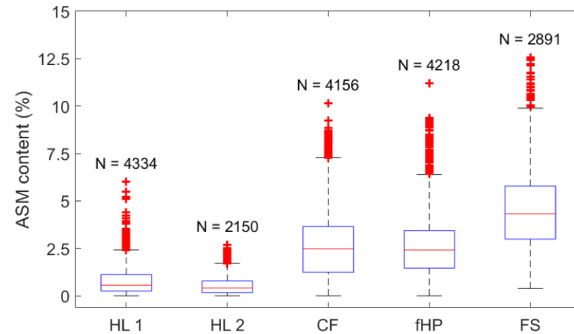


Fig. 1. Box plots of segmented ASM in all lung types (excluding COPD). The bottom of the box represents the 25th percentile, the red line represents the median, the top of the box represents the 75th percentile, and the whiskers contain all values lying less than 1.5 times the interquartile range from the box edge. Outliers outside the whisker range are indicated with a red plus sign. N represents the number of frames that are taken into the box plot, i.e. the sum of the frames in all 4×2 pullbacks.

Figure 2 shows automatically segmented ASM content for fibrotic hypersensitivity pneumonitis (fHP) and healthy lung. Images showed high reproducibility of segmented ASM between consecutive scans in the same lumen, as can be seen by comparing Fig. 2(A) to Fig. 2(B). More images of segmented ASM in different lung types can be found in the [Supplement 1](#). The

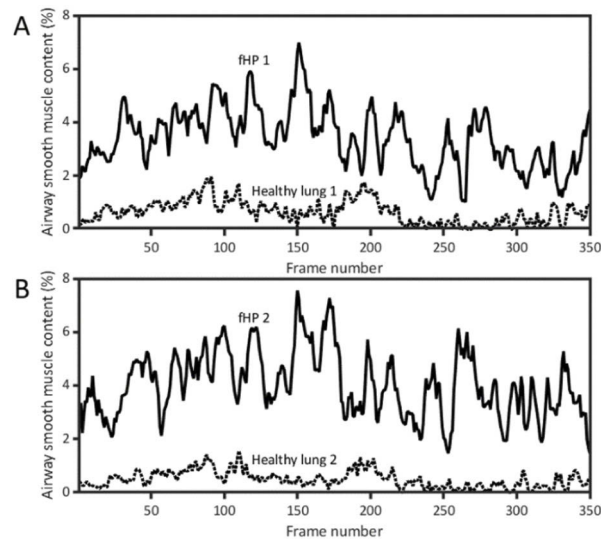


Fig. 2. Reproducibility of segmented airway smooth muscle (ASM) content in fibrotic hypersensitivity pneumonitis (fHP) and healthy lung. A) shows the first pullback in fHP and healthy lung, B) shows the consecutive pullback of the same fHP and healthy lung airway. ASM content is expressed as percentage of the full PS-OCT frame. 350 frames corresponds to approximately 14 mm pullback length.

absolute difference per frame between consecutive scans averaged over all 24 pullbacks was $0.66\% \pm 0.54\%$. The mean and median of the relative error per frame were 40% and 25%, respectively. When all frames per pullback were averaged first, the absolute difference of the mean ASM content was $0.10\% \pm 0.50\%$. The mean and median of the relative percent difference of the mean ASM content per pullback were 19% and 13%, respectively. Other image features such as alveoli and cartilages were easily recognizable between consecutive scans as well. We observed a thickened ASM cell layer in the end-stage disease tissue samples. The difference between thin ASM and thick ASM is also illustrated in Fig. 2.

Alveoli show up in the AC images as small holes with little signal. These are accompanied by an increase in signal at the tissue-air interface due to the difference in refractive index. Cartilage structures can be recognized in the AC images as a round structure with scattering material inside. They are situated deeper in the lungs, and often occur at the border of the imaging depth. A layer of collagen surrounds cartilage structures in the lungs. This layer appears as a birefringent ring in the OAxU images. Other birefringent structures in the airways are organized collagen and (collapsed) blood vessel walls. Collagen is found in various degrees of organization in histology and not clearly identifiable in the OCT images. Organized collagen may look similar to ASM in PS-OCT, and can be distinguished only if it has a different orientation. Less organized collagen shows as a patchy birefringent signal of multiple optic axis orientations.

In the next sections, PS-OCT images and histology images of the corresponding regions are shown and interpreted for every lung type. A summary of the observations in histology and PS-OCT can be found in Table 2.

Table 2. Summary of histology and PS-OCT observations

Lung type	Features observed in histology	Features observed in PS-OCT images
healthy lung	alveoli	alveoli
	little ASM	little ASM
	cartilages	cartilages
COPD	increased alveoli size	increased alveoli size
	thickened ASM	multiple layered orientations
	cartilages	cartilages
	collagen	
fibrotic sarcoidosis	little/no alveoli	no alveoli
	thickened ASM	thickened ASM
	cartilages	cartilages
	disorganized collagen	
cystic fibrosis	loss of alveoli	some alveoli
	thickened ASM	thickened (patches of) ASM
	cartilages	
	collagen	collagen (faintly)
fibrotic hypersensitivity pneumonitis	little/no alveoli	no alveoli
	thickened ASM	thickened ASM
	cartilages	cartilages
	disorganized collagen	

3.1. Healthy lung

In the healthy lung samples, two structures were easily recognizable: alveoli (Fig. 3) and cartilages (Fig. 4). The alveoli deflate at least partly in *ex vivo* samples, and are therefore smaller in diameter than when measured *in vivo* [23]. Most of the images showed only a very thin area between the lumen and alveoli (Fig. 3), in which sometimes the ASM could be recognized. However, as can be seen in the histology image (Fig. 3(A)), very little ASM was present.

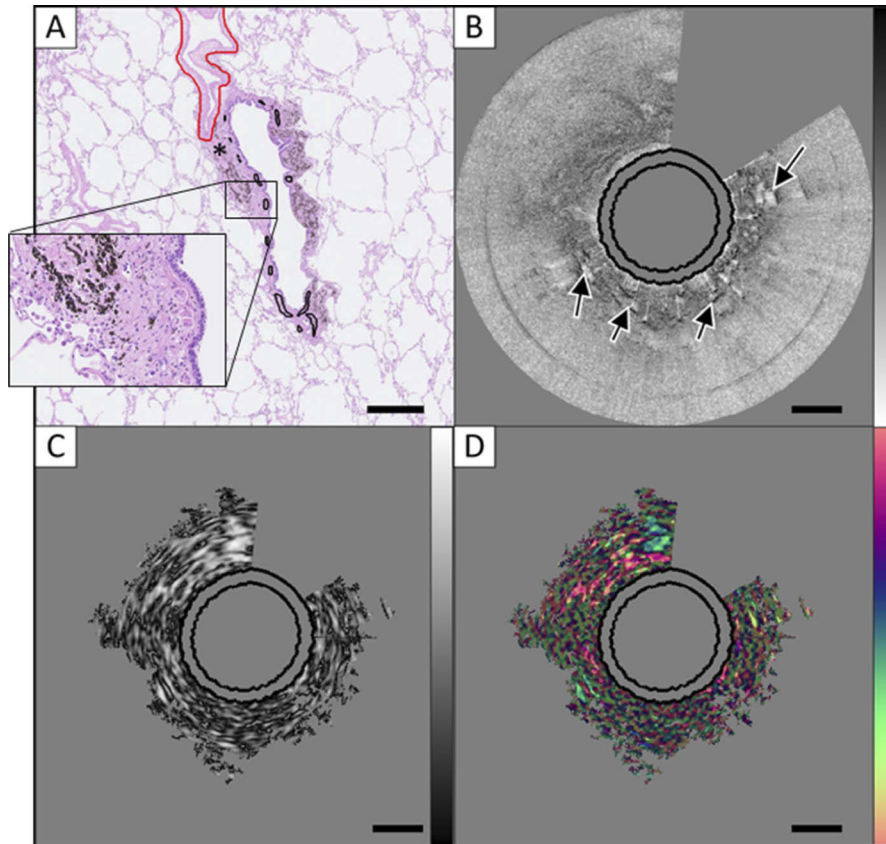


Fig. 3. Example of a bronchiolar cross section from a healthy lung sample. A) Histology image; B) AC shown on an logarithmic scale of $[10^{-1.8} \ 10^{2.7}] \text{ mm}^{-1}$ with black arrows pointing at alveoli; C) OAxU, displayed from 0 to 1; and D) relative optic axis orientation, displayed from 0 - 180°. In the histology image, ASM is delineated with black lines, a blood vessel is delineated with a red line, and a collagen region is indicated with an asterisk. Scale bars: 0.5 mm.

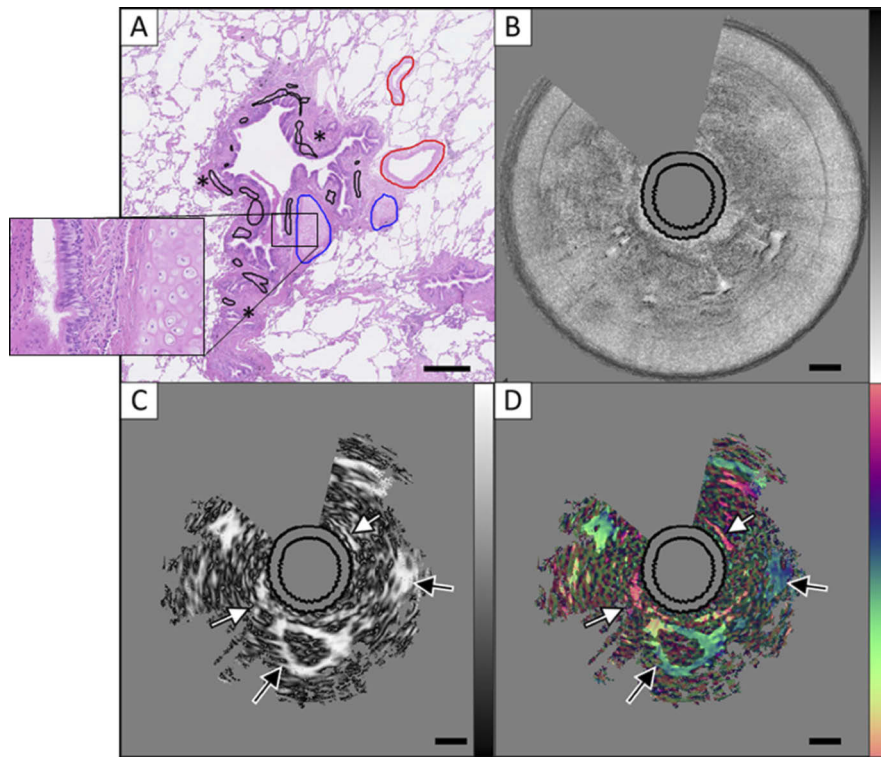


Fig. 4. Example of a bronchial cross section from a healthy lung sample showing a cartilage ring. A) Histology image; B) AC shown on a logarithmic scale of $[10^{-1.8} \ 10^{2.7}] \text{ mm}^{-1}$; C) OAxU, displayed from 0 to 1; and D) relative optic axis orientation, displayed from 0 - 180°. In the histology image, ASM is delineated with black lines, blood vessels with red lines and cartilages with blue lines. Collagen regions are indicated with an asterisk. White arrows point towards ASM and black arrows point towards cartilage in C) and D). Scale bars: 0.5 mm.

Figure 5 shows a 3D representation of the sample shown in Fig. 3. Many alveoli can be recognized in the AC image (black arrows in Fig. 5(A)). OAxU and orientation images show little amount of ASM throughout the scan. A thin line of high OAxU and pink orientation could be recognized in some frames, as indicated with white arrows in Fig. 5(B)-(C).

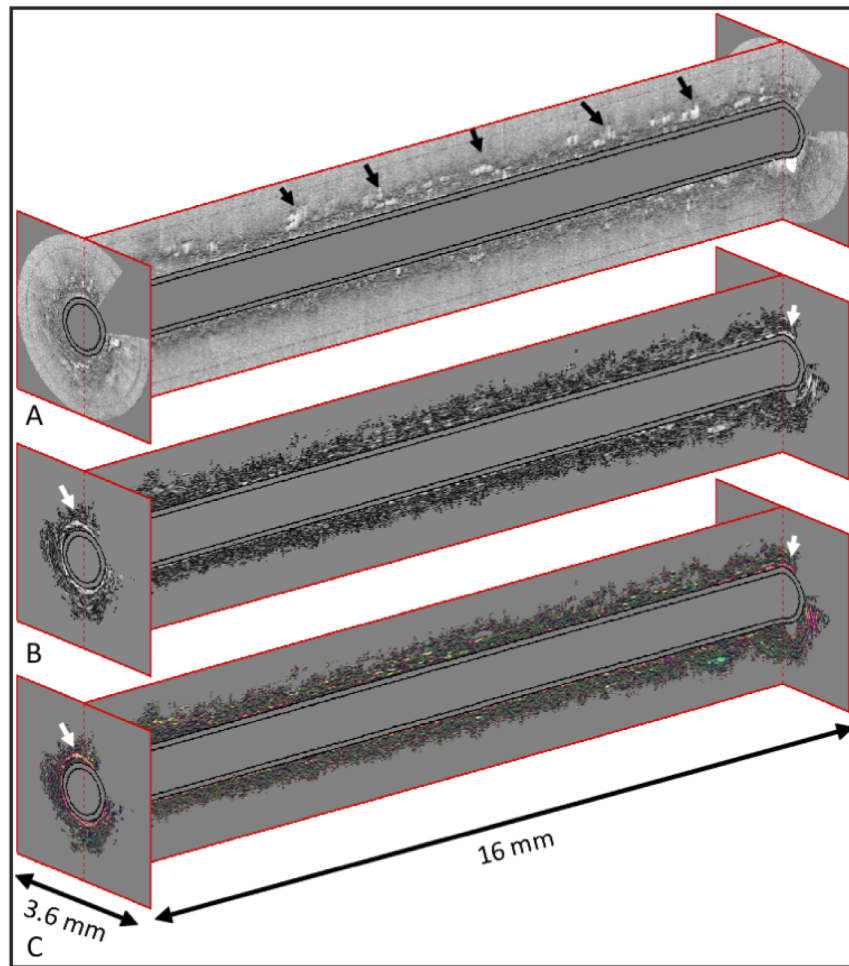


Fig. 5. Example of a healthy lung in 3D representation. A) AC image; B) OAxU image; and C) relative orientation image. Many alveoli can be recognized in A), of which a few are indicated with black arrows. ASM is very thin, but could be recognized in some frames by its high OAxU signal and pink orientation, as delineated by the white arrows in B) and C). A rotating video of this image is included in [Visualization 1](#).

3.2. COPD

In COPD, an increase in alveoli size was clearly visible. Macroscopically the tissue showed trapped air. The lung deflated when it was separated into different segments, although remaining trapped air was still clearly present. A small layer of tissue between the lumen and alveoli was observed. A normal thickness in airway wall was observed. An example of COPD histology and corresponding PS-OCT images is shown in Fig. 6.

Histological sections showed thickened ASM with mostly a nearly circumferential orientation with respect to the lumen and some with longitudinal orientation. The orientation in histology was estimated by the length of the nuclei of the smooth muscle cells.

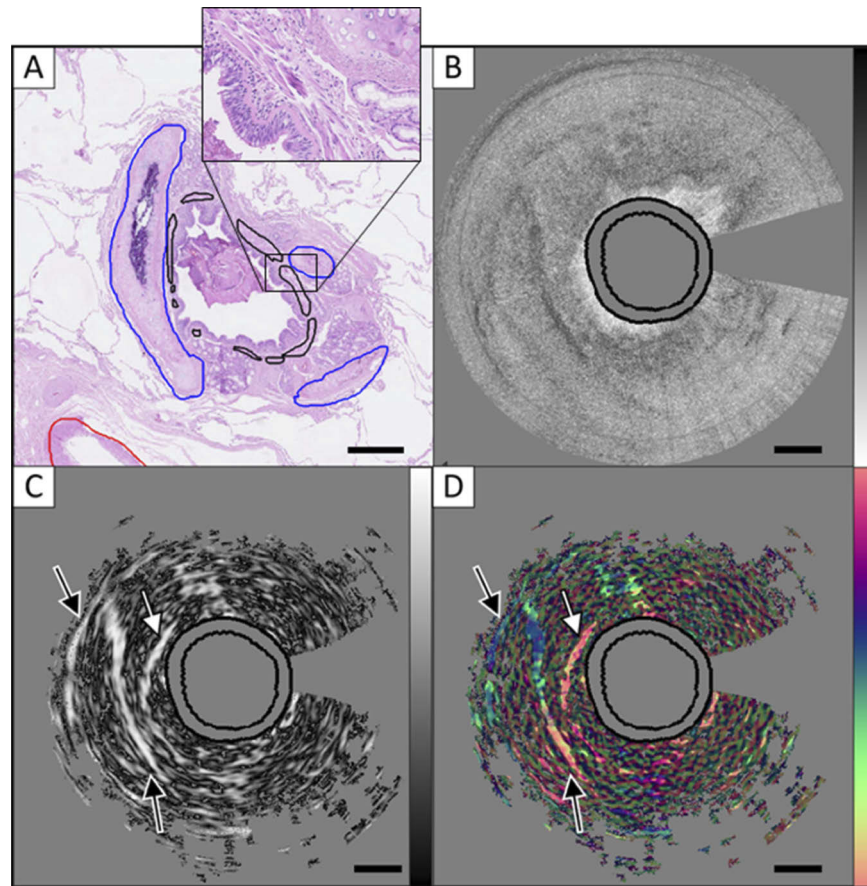


Fig. 6. Example of a bronchial cross section from a COPD sample. A) Histology image; B) AC shown on a logarithmic scale of $[10^{-1.8} \ 10^{2.7}] \text{ mm}^{-1}$; C) OAxU, displayed from 0 to 1; and D) relative optic axis orientation, displayed from 0 - 180°. In the histology image, ASM is delineated with black lines, blood vessels with red lines, and cartilages with blue lines. In the PS-OCT image the white arrow points towards ASM and black arrows point towards cartilage in C) and D). Scale bars: 0.5 mm.

Figure 7 shows a 3D representation of another airway of the same COPD lung. The attenuation coefficient image in Fig. 7(A) shows the increased alveoli size. Optic axis images (Fig. 7(C)) showed multiple orientations in three out of the four imaged airways of this lung, which assumingly correspond to both organized collagen and ASM. In the other lungs, ASM was recognized by its consistent orientation throughout the pullback. This approach does not seem to hold for this COPD lung. As can be seen in Fig. 7, a pink layer around the lumen dominates for 4.6 mm in the first, more distal region (Fig. 7(C1)). This layer disappears and is replaced by a green orientation (90° difference) for the next 5.4 mm (Fig. 7(C2)). In the last 6 mm of the section shown in Fig. 7, both green and pink layers are present (Fig. 7(C3)). Under the hypothesis that one of the two layers is ASM and the other one is fibrotic collagen, it can be concluded that the ASM is absent or too thin to be detected in at least one of these sections.

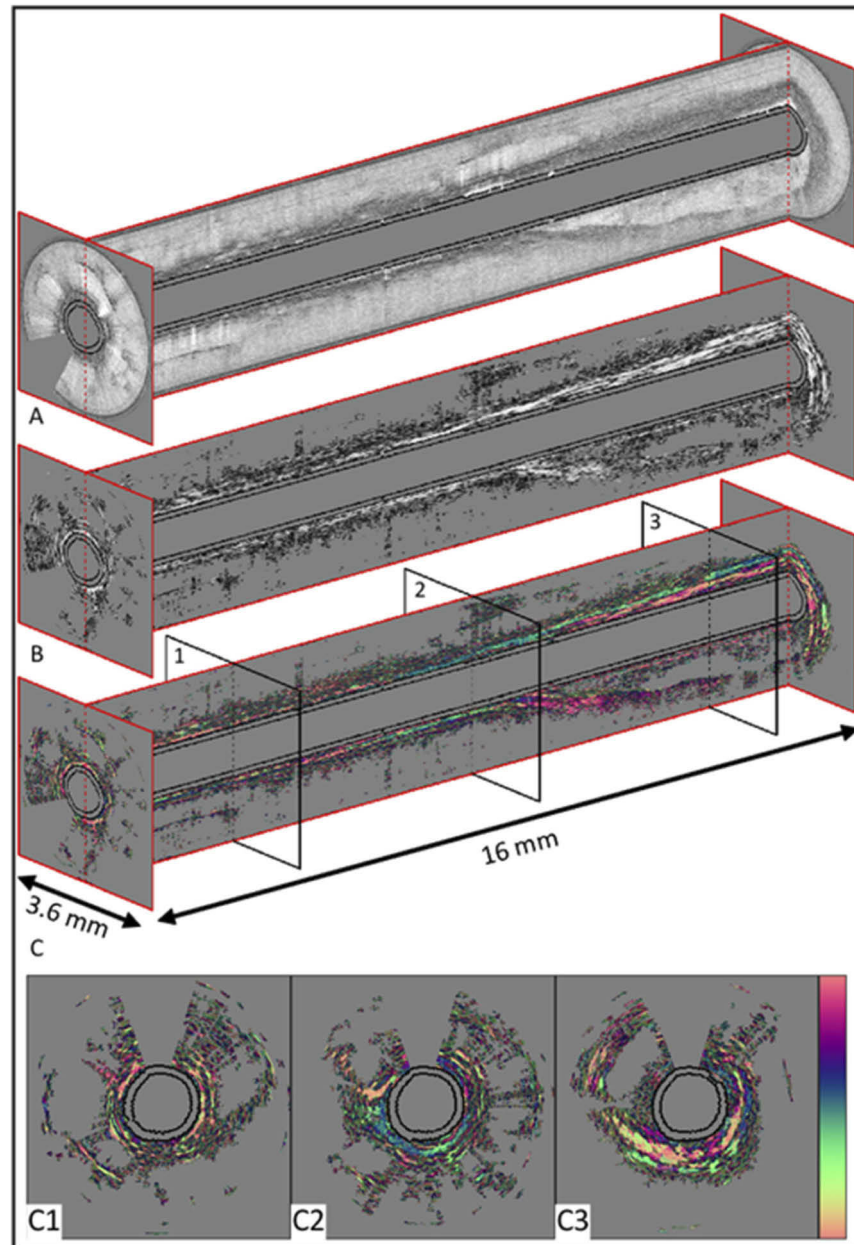


Fig. 7. Example of a COPD sample in 3D representation. A) AC image; B) OAxU image; and C) relative orientation image. Large alveoli can be recognized in A). Frames 1, 2, and 3 delineated in C) are shown in 2D in C1), C2) and C3), respectively. A rotating video of this image is included in [Visualization 2](#).

In the histology, focal collagen deposition was observed both beneath ASM (further away from the lumen) and above ASM (closer to the lumen). An example of this is shown in Fig. 8.

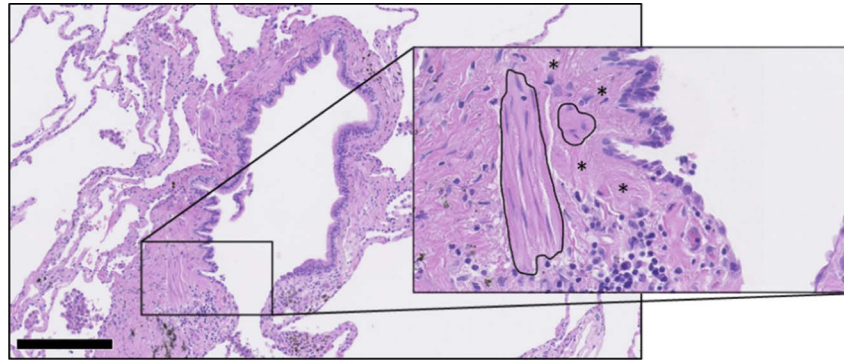


Fig. 8. Histology image of a COPD sample where focal collagen deposition was observed between the ASM and the lumen. ASM is delineated with black lines in the zoomed-in region. Collagen regions are indicated with asterisks in the zoomed-in region. Scale bar: 250 μm .

3.3. *Fibrotic hypersensitivity pneumonitis and fibrotic sarcoidosis*

Fibrotic hypersensitivity pneumonitis (fHP) and fibrotic sarcoidosis (FS) samples showed similar features. A clearly thickened ASM layer was observed in all PS-OCT and histology images. Figure 9 shows such a thickened layer (indicated with white arrows in C and D) as well as cartilage (indicated with black arrows in C and D) for fHP, which was used as a landmark to match with histology. No signals of alveoli were present in both diseased lungs due to the collapse and destruction of alveoli (Fig. 9(A), B). In addition, in the histology a lot of disorganized collagen is observed, spread-out through the tissue sample, as denoted by asterisks in Fig. 9(A). This disorganized collagen was not recognized in the PS-OCT images, possibly because it lies deeper in the tissue than the imaging range.

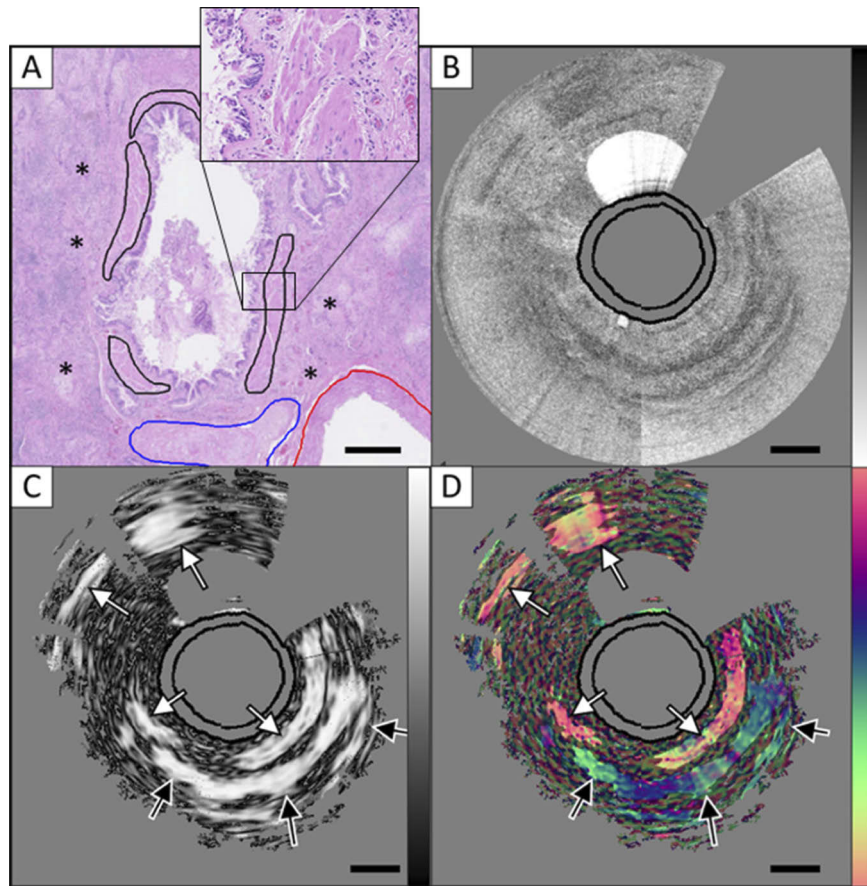


Fig. 9. Example of a bronchial cross section from a fibrotic hypersensitivity pneumonitis sample. A) Histology image; B) AC shown on a logarithmic scale of $[10^{-1.8} \ 10^{2.7}] \text{ mm}^{-1}$; C) OAxU, displayed from 0 to 1; and D) relative optic axis orientation, displayed from 0 - 180°. In histology ASM is delineated with black lines, blood vessels with red lines, cartilages with blue lines and regions containing collagen are indicated by an asterisk. In PS-OCT image white arrows point towards ASM and black arrows point towards cartilage in C) and D). Scale bars: 0.5 mm.

The thickened ASM and absence of alveoli is easier to recognize in the 3D representations, such as in the FS sample shown in Fig. 10. Figure 10(A) does not show any of the characteristic holes, but shows a rather homogeneous gray shade. OAxU images can clearly visualize ASM, as shown as white signal in Fig. 10(B), and pink orientation in Fig. 10(C). The continuous measured orientation of this band and corresponding location in the histology show that it is ASM. The signal-band was not continuous, and circled during the pullback (see Visualization 3).

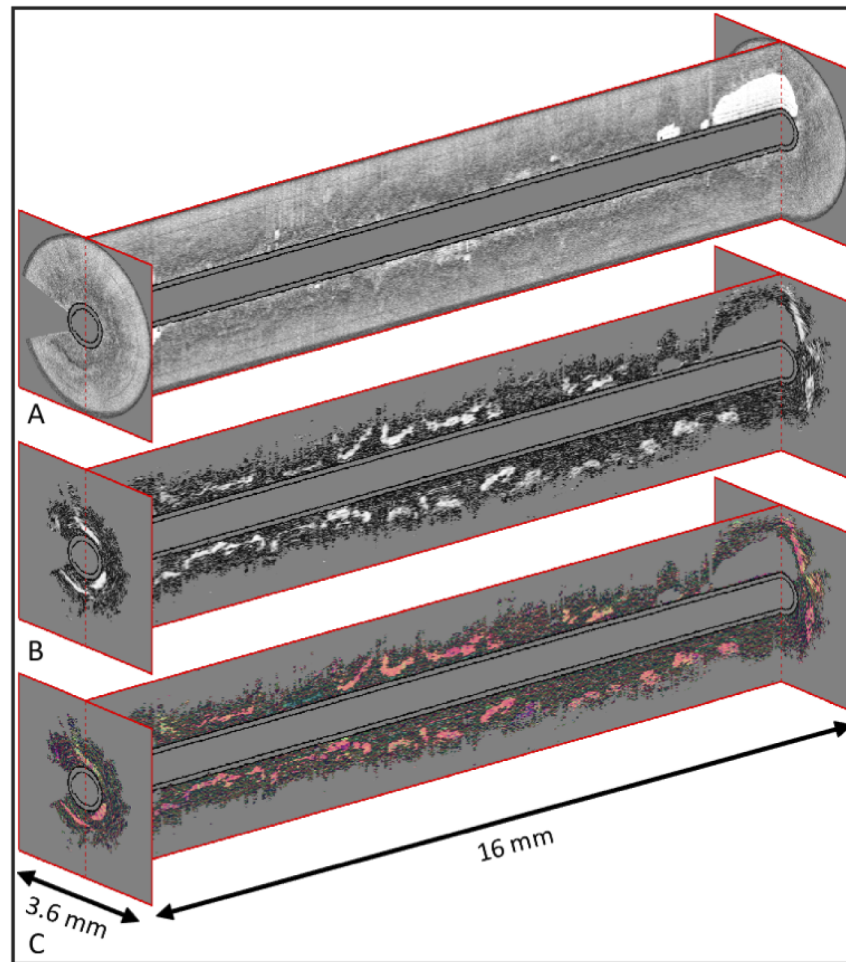


Fig. 10. Example of an FS sample in 3D representation. A) AC image; B) OAxU image; and C) relative orientation image. Alveoli are absent in A). ASM is very thick, and can be recognized by the pink color in the orientation images. A rotating video of this image is included in [Visualization 3](#).

3.4. Cystic fibrosis

Cystic fibrosis histology images showed many areas of inflammation, a thickened airway wall, a thickened ASM layer, collagen, and loss of alveoli mainly in the more proximal airways. The lung contained a lot of mucus, which made the identification of the epithelial layer difficult in the PS-OCT images. Combined with the thickened airway wall as identified from histology, the mucus layer resulted in three pullbacks with PS-OCT images where the ASM was located much deeper than in the other samples. In addition, the airway diameters were quite large (1–5 mm in diameter), and therefore tissue/ASM was not captured in all frames and was completely absent in one of the four imaged airways. The organized collagen was faintly recognizable in some of the PS-OCT images as differently oriented birefringence signal underneath the ASM. In airway 1 mostly mucus was imaged. In airway 2 a thickened ASM could be observed. In airway 3 ASM could be observed much deeper than usual. Airway 4 showed deeper thick patches of ASM.

Figure 11 shows cystic fibrosis PS-OCT images matched with histology of one of the smaller lumen measured. Histology shows the mucus inside the lumen, thickened ASM, blood vessels,

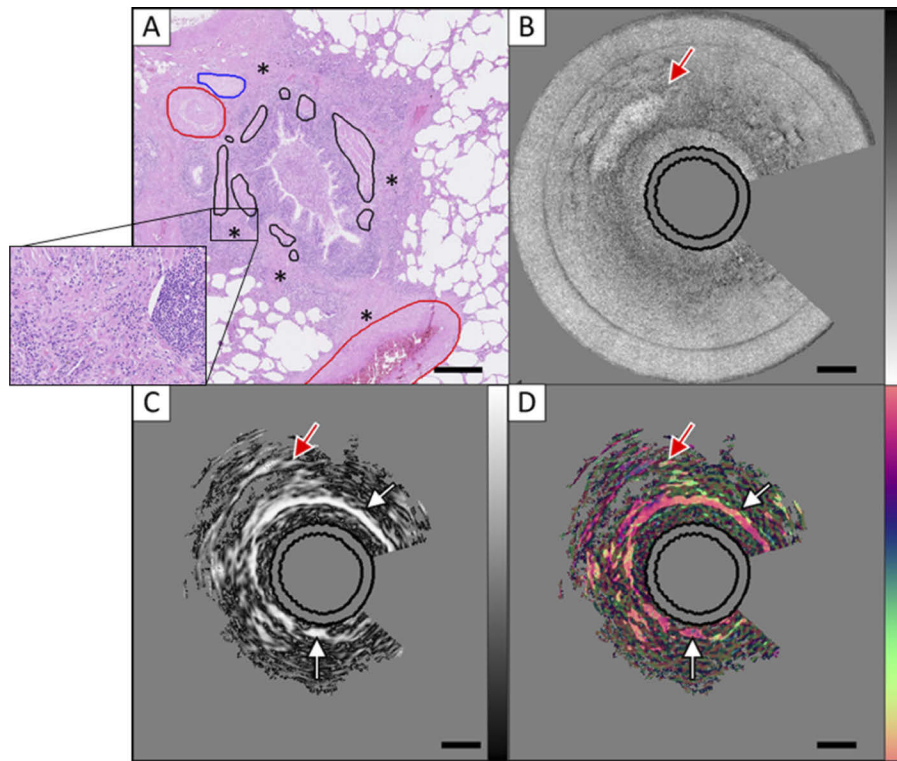


Fig. 11. Example of a cross section from a cystic fibrosis sample. A) Histology image, where ASM is delineated with black lines, blood vessels with red lines, cartilage with blue lines and collagen regions with an asterisk; B) AC shown on a logarithmic scale of $[10^{-1.8} \text{ } 10^{2.7}] \text{ mm}^{-1}$; C) OAxU, displayed from 0 to 1; and D) optic axis orientation, displayed from 0 - 180°. White arrows point towards ASM in C) and D). The red arrow points to (possibly) a blood vessel. Scale bars: 0.5 mm.

cartilage and collagen regions. PS-OCT images show the alveoli, ASM and possibly a blood vessel. Figure 12 shows the same thickened ASM and loss of alveoli throughout the pullback.

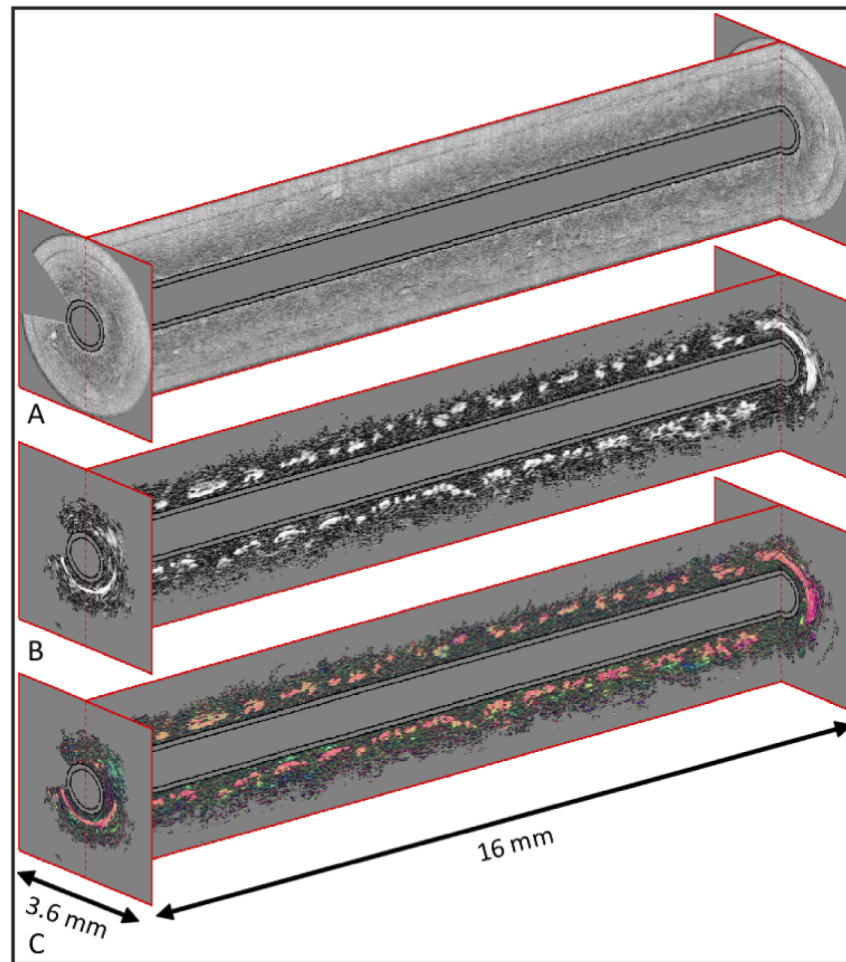


Fig. 12. Example of a cystic fibrosis sample in 3D representation. A) AC image; B) OAxU image; and C) orientation image. Alveoli are absent in A). ASM is very thick, and can be recognized by the pink color in the orientation images. A rotating video of this image is included in [Visualization 4](#).

4. Discussion

In this study, clear differences in alveoli size/presence and ASM thickness have been observed between healthy and diseased lung. ASM thickness cannot be determined using structural OCT only. This shows the additional value of polarization-sensitive measurements.

ASM segmentation showed high repeatability between two consecutive scans of the same area. In practice, the average ASM content measured in each airway will be of most interest, which was repeatable with a relative percent difference of 13%. Even though the pullback was motorized, the retraction speed of the catheter was not perfectly constant between the two measurements. This can be attributed to varying resistance inside the tissue as the catheter is pulled back multiple times, and explains the slight shift in location of the peaks observed in Fig. 2.

Even though special care was taken to label airways, matching histology to PS-OCT by visual inspection was challenging. When the lung is dissected and stained, image features can deform slightly [23], which complicates one-to-one matching. Marking tissue samples with a tissue dye

that is visible in both PS-OCT and histology [24] would have helped to better find the exact locations of both image modalities.

As the *ex vivo* samples are deflated, the images will be different from *in vivo* data, for example because of collapsed blood vessels and alveoli.

Optic axis orientation images are very useful to discriminate different birefringent structures, such as ASM from cartilage, and to provide contrast that is not available in standard OCT imaging. Contrast for cartilage and especially ASM and collagen is poor in standard OCT, but can clearly be identified with PS-OCT in OAxU and fiber orientation images. ASM was recognized as a layer with constant orientation throughout the pullbacks in all lungs except COPD. Fibrosis in the fibrotic lung diseases is less consistent in its orientation. From a clinical perspective, PS-OCT could provide a valuable method for identifying ASM thickness *in vivo*, which seems to be altered for COPD and fibrotic diseases, like fibrotic sarcoidosis, fibrotic hypersensitivity pneumonitis, and cystic fibrosis. In addition, PS-OCT could provide a noninvasive quantification of small airway ASM thickness. The small airways are the target for inhalation medication, such as beta agonists, anticholinergics and inhaled corticosteroids, such as in asthma [25] and COPD [26]. Therefore, PS-OCT might be helpful when evaluating treatments targeting airway remodeling, such as the ASM by bronchial thermoplasty in asthma patients [16] or targeted lung denervation in COPD [27].

In the current experiments, the measured optic axis orientations are relative, and no true orientation calibration could be made with the catheter used in this study. In future, homogeneously oriented birefringent material will be chosen for the catheter sheath, to be used as a calibration tool to determine the true fiber orientation in the tissue. This will also help discriminating parallel oriented from circumferentially oriented structures, as observed in for example COPD images.

A limitation of this study is the small number of samples investigated, which were all from end-stage diseased tissue. As these diseases are heterogeneous, no conclusions about pathology should be made based on this study. Rather, this pilot study shows the potential of PS-OCT to evaluate these structures. Studies with larger samples including earlier stage disease samples need to be conducted to further confirm pathological findings. This should include both *in vivo* studies and additional *ex vivo* studies with precisely matched histology.

In conclusion, multiple diseased and healthy lungs were imaged with PS-OCT and matched with histology images for the first time in this *ex vivo* study. PS-OCT might be a promising tool to measure ASM, fibrosis and other peribronchial and peribronchiolar structures *in vivo* at near micrometer resolution.

Funding. Nederlandse Organisatie voor Wetenschappelijk Onderzoek (918.10.628); Laserlab-Europe (EC-GA 654148, EC-GA 871124); Heidelberg Engineering.

Acknowledgments. The authors would like to thank Jelmer Weda (Vrije Universiteit) and Helene Knaus (University Utrecht) for their help with acquiring the data.

Disclosures. JFdB: Terumo, inc., Heidelberg Engineering, Spectrawave. (P, R),

Data availability. Data underlying the results presented in this paper are not publicly available at this time but may be obtained from the authors upon reasonable request within 5 years after publication date.

Supplemental document. See [Supplement 1](#) for supporting content.

References

1. H. O. Coxson, B. Quiney, D. D. Sin, L. Xing, A. M. McWilliams, J. R. Mayo, and S. Lam, "Airway wall thickness assessed using computed tomography and optical coherence tomography," *Am. J. Respir. Crit. Care Med.* **177**(11), 1201–1206 (2008).
2. S. Lam, B. Standish, C. Baldwin, A. McWilliams, A. Gazdar, A. I. Vitkin, V. Yang, N. Ikeda, and C. MacAulay, "In vivo optical coherence tomography imaging of preinvasive bronchial lesions," *Clin. Cancer Res.* **14**(7), 2006–2011 (2008).
3. R. G. Michel, G. T. Kinasewitz, K.-M. Fung, and J. I. Keddissi, "Optical coherence tomography as an adjunct to flexible bronchoscopy in the diagnosis of lung cancer: a pilot study," *Chest* **138**(4), 984–988 (2010).

4. L. P. Hariri, M. B. Applegate, M. Mino-Kenudson, E. J. Mark, B. D. Medoff, A. D. Luster, B. E. Bouma, G. J. Tearney, and M. J. Suter, "Volumetric optical frequency domain imaging of pulmonary pathology with precise correlation to histopathology," *Chest* **143**(1), 64–74 (2013).
5. M. Ding, Y. Chen, W.-J. Guan, C.-H. Zhong, M. Jiang, W.-Z. Luo, X.-B. Chen, C.-L. Tang, Y. Tang, and Q.-M. Jian, "Measuring airway remodeling in patients with different COPD staging using endobronchial optical coherence tomography," *Chest* **150**(6), 1281–1290 (2016).
6. D. C. Adams, A. J. Miller, M. B. Applegate, J. L. Cho, D. L. Hamilos, A. Chee, J. A. Holz, M. V. Szabari, L. P. Hariri, and R. S. Harris, "Quantitative assessment of airway remodelling and response to allergen in asthma," *Respirology* **24**(11), 1073–1080 (2019).
7. L. P. Hariri, D. C. Adams, J. C. Wain, M. Lanuti, A. Muniappan, A. Sharma, T. V. Colby, M. Mino-Kenudson, E. J. Mark, and R. L. Kradin, "Endobronchial optical coherence tomography for low-risk microscopic assessment and diagnosis of idiopathic pulmonary fibrosis in vivo," *Am. J. Respir. Crit. Care Med.* **197**(7), 949–952 (2018).
8. S. Nandy, R. A. Raphaely, A. Muniappan, A. Shih, B. W. Roop, A. Sharma, C. M. Keyes, T. V. Colby, H. G. Auchincloss, and H. A. Gaissert, "Diagnostic accuracy of endobronchial optical coherence tomography for the microscopic diagnosis of usual interstitial pneumonia," *Am. J. Respir. Crit. Care Med.* (2021).
9. M. R. Hee, D. Huang, E. A. Swanson, and J. G. Fujimoto, "Polarization-sensitive low-coherence reflectometer for birefringence characterization and ranging," *J. Opt. Soc. Am. B* **9**(6), 903–908 (1992).
10. J. F. de Boer, T. E. Milner, M. J. van Gemert, and J. S. Nelson, "Two-dimensional birefringence imaging in biological tissue by polarization-sensitive optical coherence tomography," *Opt. Lett.* **22**(12), 934–936 (1997).
11. B. H. Park, M. C. Pierce, B. Cense, and J. F. de Boer, "Optic axis determination accuracy for fiber-based polarization-sensitive optical coherence tomography," *Opt. Lett.* **30**(19), 2587–2589 (2005).
12. L. P. Hariri, M. Villiger, M. B. Applegate, M. Mino-Kenudson, E. J. Mark, B. E. Bouma, and M. J. Suter, "Seeing beyond the bronchoscope to increase the diagnostic yield of bronchoscopic biopsy," *Am. J. Respir. Crit. Care Med.* **187**(2), 125–129 (2013).
13. L. P. Hariri, D. C. Adams, M. B. Applegate, A. J. Miller, B. W. Roop, M. Villiger, B. E. Bouma, and M. J. Suter, "Distinguishing tumor from associated fibrosis to increase diagnostic biopsy yield with polarization-sensitive optical coherence tomography," *Clin. Cancer Res.* **25**(17), 5242–5249 (2019).
14. D. C. Adams, L. P. Hariri, A. J. Miller, Y. Wang, J. L. Cho, M. Villiger, J. A. Holz, M. V. Szabari, D. L. Hamilos, R. S. Harris, J. W. Griffith, B. E. Bouma, A. D. Luster, B. D. Medoff, and M. J. Suter, "Birefringence microscopy platform for assessing airway smooth muscle structure and function in vivo," *Sci. Transl. Med.* **8**(359), 359ra131 (2016).
15. D. C. Adams, J. A. Holz, M. V. Szabari, L. P. Hariri, A. F. McCrossan, C. J. Manley, S. Fleury, S. O'Shaughnessy, J. Weiner, and M. J. Suter, "In vivo assessment of changes to canine airway smooth muscle following bronchial thermoplasty with OR-OCT," *J. Appl. Physiol.* **130**(6), 1814–1821 (2021).
16. M. Vaselli, P. Wijsman, J. Willemse, A. Goorsenberg, F. Feroldi, J. d'Hooghe, J. Annema, J. de Boer, and P. Bonta, "Polarization sensitive optical coherence tomography (PS-OCT) for bronchoscopic airway smooth muscle detection in bronchial thermoplasty treated asthma patients," *Chest* (2021).
17. F. Feroldi, J. Willemse, V. Davidoiu, M. G. Gräfe, D. J. van Iperen, A. W. Goorsenberg, J. T. Annema, J. M. Daniels, P. I. Bonta, and J. F. de Boer, "In vivo multifunctional optical coherence tomography at the periphery of the lungs," *Biomed. Opt. Express* **10**(6), 3070–3091 (2019).
18. K. A. Vermeer, J. Mo, J. J. Weda, H. G. Lemij, and J. F. de Boer, "Depth-resolved model-based reconstruction of attenuation coefficients in optical coherence tomography," *Biomed. Opt. Express* **5**(1), 322–337 (2014).
19. M. Villiger, D. Lorensen, R. A. McLaughlin, B. C. Quirk, R. W. Kirk, B. E. Bouma, and D. D. Sampson, "Deep tissue volume imaging of birefringence through fibre-optic needle probes for the delineation of breast tumour," *Sci. Rep.* **6**(1), 28771 (2016).
20. J. Willemse, M. G. Gräfe, F. D. Verbraak, and J. F. de Boer, "In vivo 3D determination of peripapillary scleral and retinal layer architecture using polarization-sensitive optical coherence tomography," *Trans. Vis. Sci. Tech.* **9**(11), 21 (2020).
21. J. Willemse, M. G. Gräfe, J. A. van de Kreeke, F. Feroldi, F. D. Verbraak, and J. F. de Boer, "Optic axis uniformity as a metric to improve the contrast of birefringent structures and analyze the retinal nerve fiber layer in polarization-sensitive optical coherence tomography," *Opt. Lett.* **44**(15), 3893–3896 (2019).
22. D. C. Adams, M. V. Szabari, D. Lagares, A. F. McCrossan, L. P. Hariri, A. M. Tager, and M. J. Suter, "Assessing the progression of systemic sclerosis by monitoring the tissue optic axis using PS-OCT," *Sci. Rep.* **10**(1), 1–10 (2020).
23. E. Thunnissen, H. J. Blaauwgeers, E. M. de Cuba, C. Y. Yick, and D. B. Flieder, "Ex vivo artifacts and histopathologic pitfalls in the lung," *Arch. Pathol. Lab. Med.* **140**(3), 212–220 (2016).
24. L. P. Hariri, M. B. Applegate, M. Mino-Kenudson, E. J. Mark, B. E. Bouma, G. J. Tearney, and M. J. Suter, "Optical frequency domain imaging of ex vivo pulmonary resection specimens: obtaining one to one image to histopathology correlation," *JoVE (Journal of Visualized Experiments)*, e3855 (2013).
25. L.-P. Boulet, H. K. Reddel, E. Bateman, S. Pedersen, J. M. FitzGerald, and P. M. O'Byrne, "The global initiative for asthma (GINA): 25 years later," *Eur. Respir. J.* **54**(2), 1900598 (2019).
26. "COPD GOLD guidelines," www.copdgold.org.
27. D.-J. Slebos, K. Klooster, C. F. Koegelenberg, J. Theron, D. Styen, A. Valipour, M. Mayse, and C. T. Bolliger, "Targeted lung denervation for moderate to severe COPD: a pilot study," *Thorax* **70**(5), 411–419 (2015).